CHEMISTRY OF MATERIALS

pubs.acs.org/cm

Article

Artificial Intelligence to Accelerate the Discovery of N_2 Electroreduction Catalysts

Myungjoon Kim,[§] Byung Chul Yeo,[§] Youngtae Park, Hyuck Mo Lee, Sang Soo Han,* and Donghun Kim*

Cite This: https://dx.doi.org/10.1021/acs.chemmater.9b03686

Read Online

ACCESS | Metrics & More | Article Recommendations | Supporting Information

ABSTRACT: The development of catalysts for the electrochemical N_2 reduction reaction (NRR) with a low limiting potential and high Faradaic efficiency is highly desirable but remains challenging. Here, to achieve acceleration, we develop and report a slab graph convolutional neural network (SGCNN), an accurate and flexible machine learning (ML) model that is suited for probing surface reactions in catalysis. With a self-accumulated database of 3040 surface calculations at the density-functional-theory (DFT) level, SGCNN predicted the binding energies, ranging over 8 eV, of five key adsorbates (H, N_2, N_2H, NH, NH_2) related to NRR performance with a mean absolute error (MAE) of only 0.23 eV. SGCNN only requires the low-level inputs of elemental properties available in the periodic table of elements and connectivity information of constituent atoms; thus, accelerations can be realized. Via a combined process of SGCNN-driven predictions and DFT verifications, four novel catalysts in the $L1_2$ crystal space, including $V_3Ir(111)$, $Tc_3Hf(111)$, $V_3Ni(111)$, and $Tc_3Ta(111)$, are proposed as stable candidates that likely exhibit both a lower limiting potential and higher Faradaic efficiency in the NRR, relative to the reference Mo(110). The ML work combined with a statistical data analysis reveals that catalytic surfaces with an average d-orbital occupation between 4 and 6 could lower the limiting potential and potentially overcome the scaling relation in the NRR.

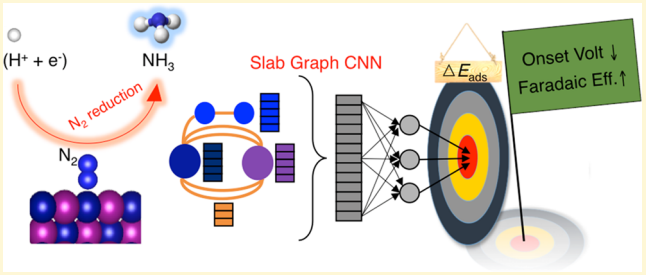

INTRODUCTION

Copious amounts of ammonia (NH_3), the major component of fertilizer, are produced globally (>145 million tons/year).[1] Currently, NH_3 production relies heavily on the energy-intensive, methane-based Haber−Bosch process (HBP). The HBP requires very harsh conditions (pressure 150−200 atm; temperature 300−500 °C) using pure hydrogen, which is mostly sourced from natural gas via steam reforming.[2,3] As a result, ammonia production today contributes significantly to greenhouse gas emissions and climate change. As an alternative to conventional HBP, the electrochemical reduction of N_2 to NH_3 has recently been pursued, as it offers more energy-efficient and eco-friendly (no CO_2 emission) production routes.[4−8]

Tremendous efforts have recently been made to develop catalysts for the electrochemical N_2 reduction reaction (NRR). A variety of catalysts have been studied both theoretically and experimentally, such as Ru,[9,10] Fe,[5] Fe_2O_3,[11,12] Au,[13−15] N-doped carbon,[16,17] and nitride monolayers,[18,19] but the ammonia production rates obtained with these catalysts are far from satisfactory (on the order of tens of ug_{NH_3}/mg_{cat}^{-1} h^{-1}). In addition, the NRR suffers from low Faradaic efficiencies (selectivity), mainly due to the competing hydrogen evolution reaction (HER). Many recent reports quantitatively compare the energetics between the NRR and HER[20] and suggest approaches to suppress the HER, which include controlling the ligands in molecular catalysts,[21] screening over single-atom catalysts,[22] and designing new electrolytes.[23] Despite these strategies, NRR is still plagued by low Faradaic efficiencies, typically much less than 30%. In light of these studies, the development of more productive and selective catalysts for the NRR is highly desired but remains slow and challenging.

Examining the potential catalyst material space via high-throughput experiments and/or first-principles calculations is costly enough to be practically impossible. To overcome this limitation, machine learning (ML) has recently emerged as a powerful and complementary tool to potentially accelerate new material discovery.[24−33] ML models have been developed to disentangle the complex catalyst−adsorbate interactions for various reactions, including CO_2 reduction,[24−26,28−30] C−C cross-coupling reactions,[27] NO decomposition,[32] and syngas reactions;[33] however, an ML model for the NRR has yet to be developed. In addition, the utility of these models for screening

Received: September 9, 2019
Revised: December 26, 2019
Published: December 27, 2019

remains challenging from two perspectives. First, many models incorporate ab initio-level (e.g., density functional theory (DFT)) surface features, such as d-band characteristics, as key inputs, which require additional DFT calculations to prepare the ML input; thus, ML-driven acceleration has not been realized. Second, the previous ML models are trained only for a specific type of crystal structure or adsorbate; no universal model capable of probing various catalytic reactions is available yet.

Herein, we adopt a graph-based convolutional neural network (GCNN) to overcome the aforementioned limitations. In the GCNN scheme, material structures are flexibly encoded into graphs whose vertices and edges correspond to feature vectors of atoms and bonds. Indeed, the graph representation in ML has been successfully applied to molecular systems[34−37] and bulk solids.[38−40] However, the application of this approach to surface−adsorbate systems, in which catalytic reactions are typically modeled, remains nonexistent. In this article, we first develop and report a slab graph convolutional neural network (SGCNN) that is applicable to surface reactions in catalysis. SGCNN overcomes the limitations of previously available models. First, SGCNN only requires the inputs of elemental properties available in the periodic table of elements and connectivity information of constituent atoms; thus, ML-driven accelerations in catalyst development can be realized. Second, owing to the flexible graph-based encoding of structural information, SGCNN can be developed as a universal model that is applicable to diverse types of catalysts and adsorbates.

With our own database of 3040 surface DFT calculations, SGCNN predicts the binding energies, ranging over 8 eV, of five adsorbates (H, N_2, N_2H, NH, and NH_2) that are directly related to NRR performance with a mean absolute error (MAE) of only 0.23 eV. Through a sequential process of SGCNN-driven screening and DFT verification, we propose four novel catalysts in the $L1_2$ crystal space, including $V_3Ir(111)$, $Tc_3Hf(111)$, $V_3Ni(111)$, and $Tc_3Ta(111)$, that satisfy the requirements of negative formation energy (stability), a low limiting potential, and high Faradaic efficiency. The ML work combined with statistical data analysis suggests that catalytic surfaces with an average d-orbital occupation between 4 and 6 could potentially lower the limiting potential of the NRR. To the best of our knowledge, this work is the first demonstration that ML accelerated the identification of improved catalysts for ammonia production. The catalysis communities researching other chemical reactions may benefit from the SGCNN-based workflow.

RESULTS

Adsorption Energies as NRR Performance Descriptors. Out of three possible associative NRR mechanisms (distal, alternating, and enzymatic),[19,41,42] the distal pathway ($*N_2 \rightarrow *NNH \rightarrow *NNH_2 \rightarrow *N \rightarrow *NH \rightarrow *NH_2 \rightarrow *NH_3$) is dominant in flat slab models composed of transition metals, as shown in previous studies[43,44] and our own calculations (Figure S1), and thus focused on in this work. Two NRR properties are studied, i.e., (1) the limiting potential and (2) the Faradaic efficiency (or selectivity). Regarding the limiting potential, recent studies on the NRR over low-index surfaces of various pure metals suggest that one of the following two protonation steps governs the limiting potential:[43,44,45] $*N_2 + H^+ + e^- \rightarrow *N_2H$ ($*N_2 \rightarrow *N_2H$ hereafter) vs $*NH + H^+ + e^- \rightarrow *NH_2$ ($*NH \rightarrow *NH_2$ hereafter). DFT-computed free energy (ΔG) diagrams for associative NRR pathways on Ru(001) and Mo(110) are shown in Figure 1a. The details of the free energy corrections are elaborated in the Methods section and Table S1. The two

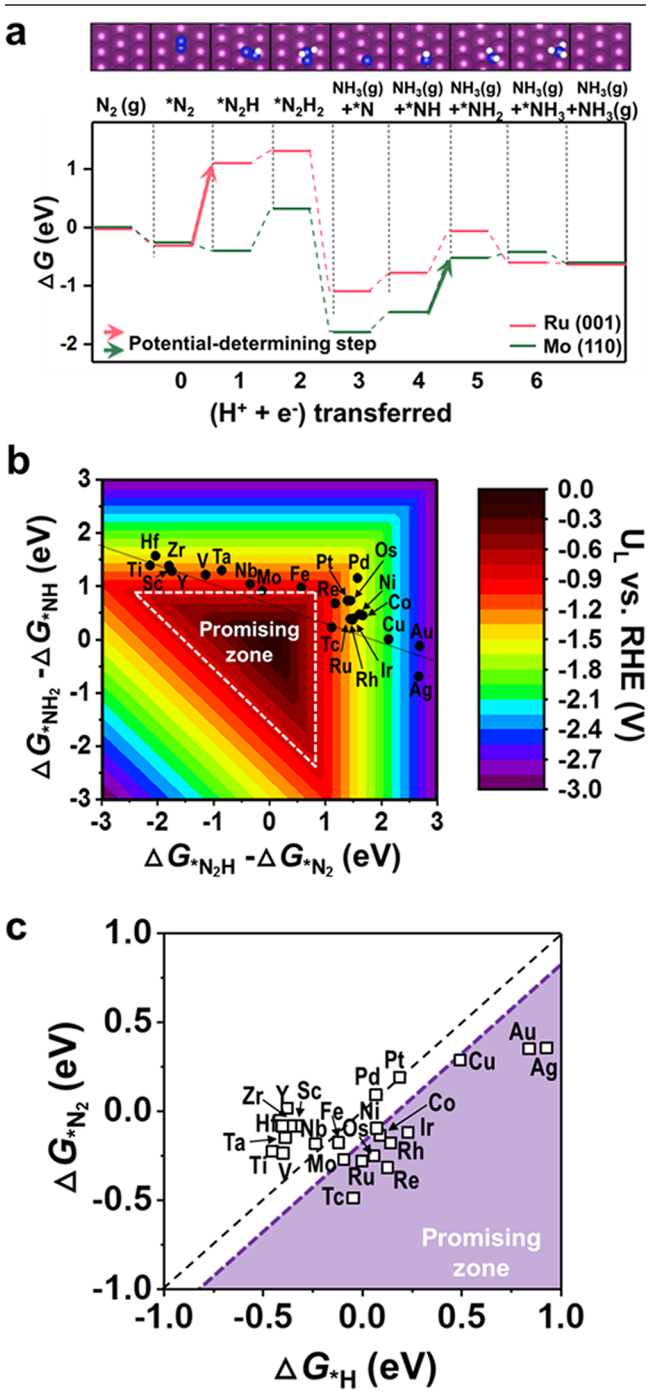

Figure 1. Adsorption energies as NRR performance descriptors. (a) Free energy (ΔG) diagrams for associative NRR pathways on Ru(001) and Mo(110). PDSs are highlighted with arrows. Corresponding surface/adsorbate structures are shown on top with blue, white, and purple atoms representing N, H, and Ru (or Mo). (b) Two-dimensional (2D) contour plot of U_L as a function of potential limiting steps for two cases ($*N_2 + H^+ + e^- \rightarrow *N_2H$ vs $*NH + H^+ + e^- \rightarrow *NH_2$). The calculation results obtained for 23 transition metals (close-packed surface) are added on the map. (c) Comparison of the free energies of N_2 and H adsorbates for 23 transition metals. Promising zones in both (b) and (c) are referenced to Mo(110).

https://dx.doi.org/10.1021/acs.chemmater.9b03686
Chem. Mater. XXXX, XXX, XXX−XXX

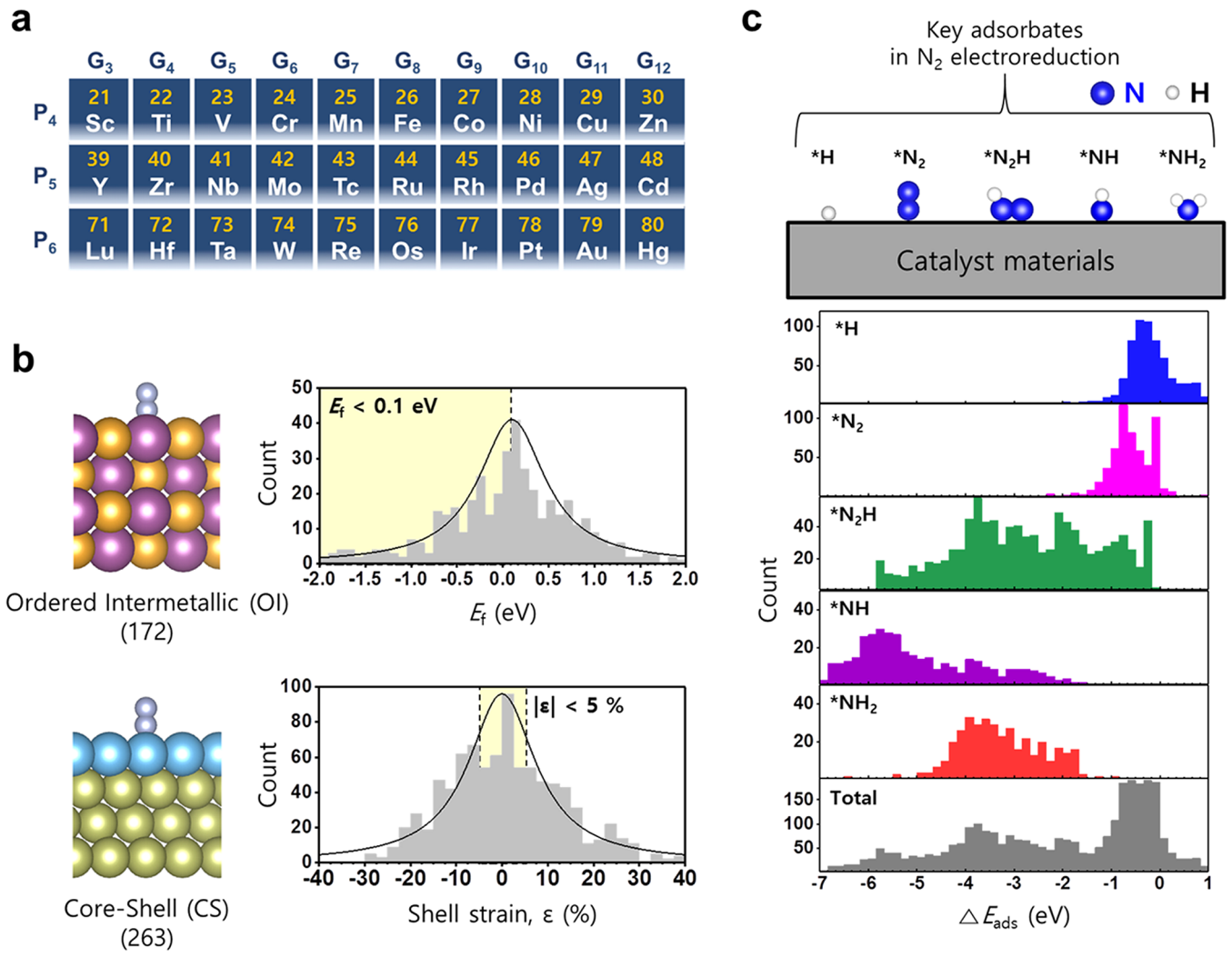

Figure 2. Database generation. (a) A portion of the periodic table of elements (GRs 3−12 and PRs 4−6). (b) Two types of binary catalyst systems (172 OIs and 263 CS systems). An example structure and distributions (over E_f for OI type and ε for CS type) are shown. For both types, samples shaded in yellow are selected for DFT surface calculations. (c) Schematic of the catalytic system with five key adsorbates in the NRR (upper). Binding energy populations ($\Delta E_{ads.}$) for each adsorbate (lower).

surfaces of Ru(001) and Mo(110) are shown as examples for each potential-determining step (PDS), $*N_2 \rightarrow *N_2H$ and $*NH \rightarrow *NH_2$. The free energy diagrams of other metal cases are available in Figure S2. For each transition metal, the most stable, low-index surface is selected: (111) for fcc, (110) for bcc, and (001) for hcp metals. All of these calculations reveal that the PDS is $*N_2 \rightarrow *N_2H$ for most late transition metals (group numbers (GRs) 7−11, e.g., Fe, Ru, Rh, Ni, Pd), but it is $*NH \rightarrow *NH_2$ for most early transition metals (GRs 3−6, e.g., Sc, Ti, Mo), which agrees with the literature.[43,44]

The minimum applied voltage required to make the NRR pathway exergonic in all steps is defined as the limiting potential (U_L). The energetics presented in Figure 1b assume that the PDS is either $*N_2 \rightarrow *N_2H$ or $*NH \rightarrow *NH_2$, and U_L is determined as the negative of the maximum of $(\Delta G_{N_2H}-\Delta G_{N_2})$ and $(\Delta G_{NH_2}-\Delta G_{NH})$, divided by the electron charge (e). The U_L values of 23 metal surfaces are marked on the map in Figure 1b, confirming a known scaling relation.[43] It should be noted that a strategy to overcome the scaling relation is critical to discover improved catalysts, but such a strategy has yet to be developed. Of the 23 metal surfaces, Mo(110) exhibits the lowest $|U_L|$ of 0.92 V, and most others exhibit $|U_L|$ values higher than 1.0 V. Our finding that Mo(110) has the lowest $|U_L|$ among transition metals is consistent with previously reported theoretical evaluations for the NRR,[43,44] although no experimental reports of Mo for the NRR are yet available due to notorious oxidation issues. We highlight the promising zone of $-0.92\ V < U_L \leq 0\ V$, as any materials positioned in this zone would require a smaller limiting potential than Mo(110) does.

The other important property for the NRR is Faradaic efficiency. The Faradaic efficiencies of previously studied catalysts are very low (typically much below 30%), mainly due to competition with the HER. In this context, the binding energy difference between $*N_2$ and *H, defined as $F = \Delta G_{N_2} - \Delta G_H$, on catalyst surfaces can serve as an excellent descriptor to estimate adsorption competitions of N_2 and H species and consequently to determine Faradaic efficiency.[22] The more negative F is for a catalyst material, the higher Faradaic efficiency the material likely exhibits. Figure 1c compares the DFT-computed ΔG_{N_2} and ΔG_H values of 23 transition metals. Here, we also define a promising zone of F less than −0.18 eV (Mo(110) value). Note that a few other surfaces, including

https://dx.doi.org/10.1021/acs.chemmater.9b03686
Chem. Mater. XXXX, XXX, XXX−XXX

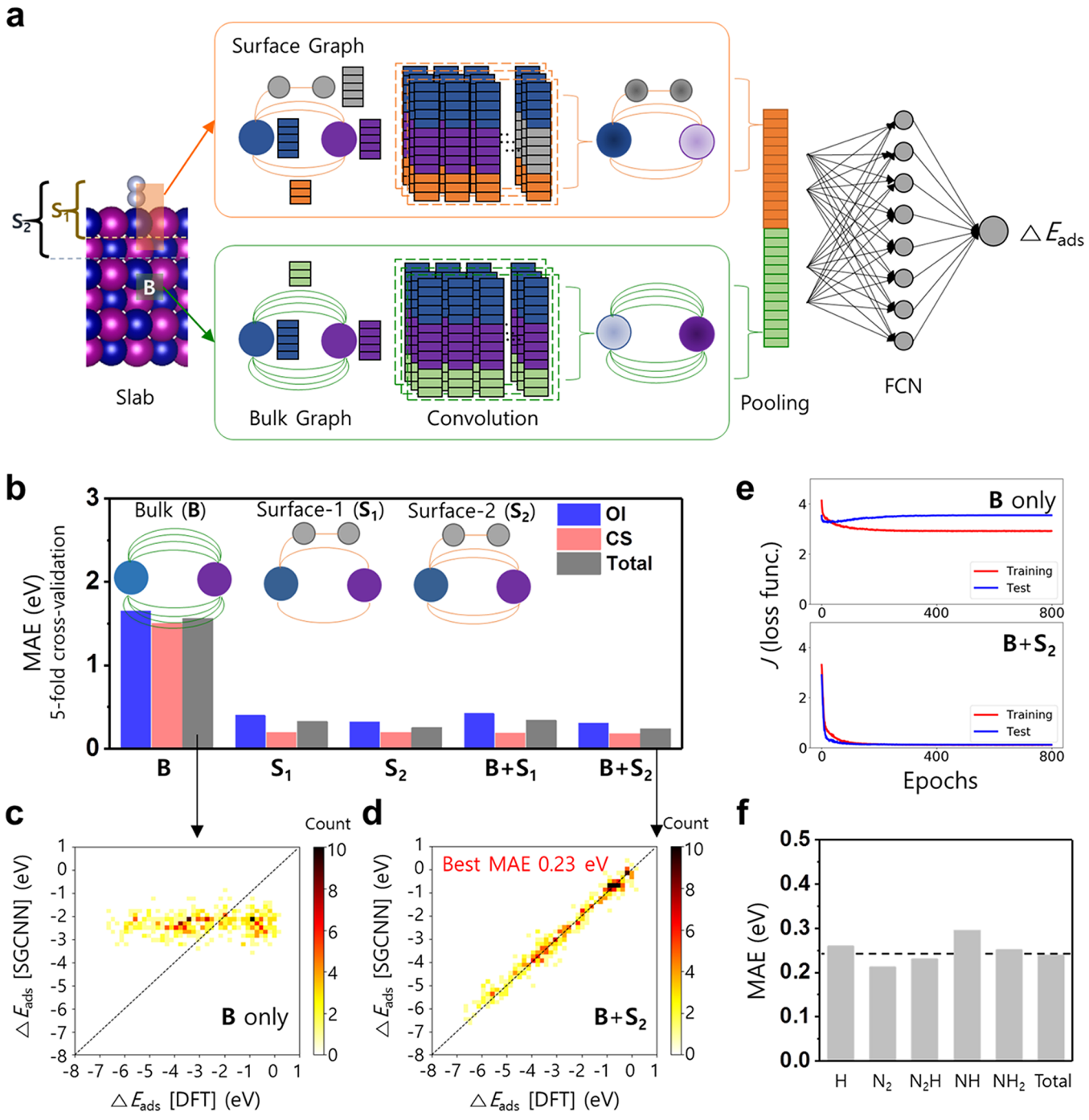

Figure 3. SGCNN development and performance. (a) Schematic describing the main architecture of the SGCNN model. Each **B** and $\mathbf{S_1}$ (or $\mathbf{S_2}$) represent the bulk graph and surface graph with the top layer (or top two layers), respectively. Method (b) Comparison of MAE values for five different graph structures (**B**, $\mathbf{S_1}$, $\mathbf{S_2}$, **B** + $\mathbf{S_1}$, and **B** + $\mathbf{S_2}$). (c, d) 2D histogram comparing the predicted adsorption energies using the SGCNN model and DFT computation: (c) case in which only the bulk graph is used and (d) case in which **B** and $\mathbf{S_2}$ are simultaneously used (**B** + $\mathbf{S_2}$). (e) Evolution of loss function, *J*, with increasing number of training steps (epochs). (f) Comparison of MAE values for H, N_2, N_2H, NH, and NH_2 adsorbates, with the dashed line representing the MAE of the total.

Ag(111) and Au(111), are better than Mo(110) in the *F* criterion; however, the limiting potentials of these elements are too high to be effective for the NRR.

Database Generation. The foregoing analysis indicates that the binding energies of five adsorbates (H, N_2, N_2H, NH, and NH_2) are directly related to NRR performance. Using DFT surface calculations, we generated our own database of 3040 binding energies for these five adsorbates as shown in Figure 2. A total of 465 catalysts are modeled in a slab geometry, including 30 unary and 435 binary systems. The binary systems are either ordered intermetallics (OIs) or core−shell (CS)-type alloys composed of transition-metal elements in period numbers (PRs) 4−6 and GRs 3−12 in the periodic table of elements (Figure 2a,b). The catalyst systems are selectively chosen as follows. Binary OIs have either $L1_0$ or B2 crystal structures with low bulk formation energy, i.e., $E_f < 0.1$ eV (172 systems). CS-type alloys are built in the most stable crystal structure of core elements (fcc, bcc, or hcp) with $|\varepsilon| <$

https://dx.doi.org/10.1021/acs.chemmater.9b03686
Chem. Mater. XXXX, XXX, XXX−XXX

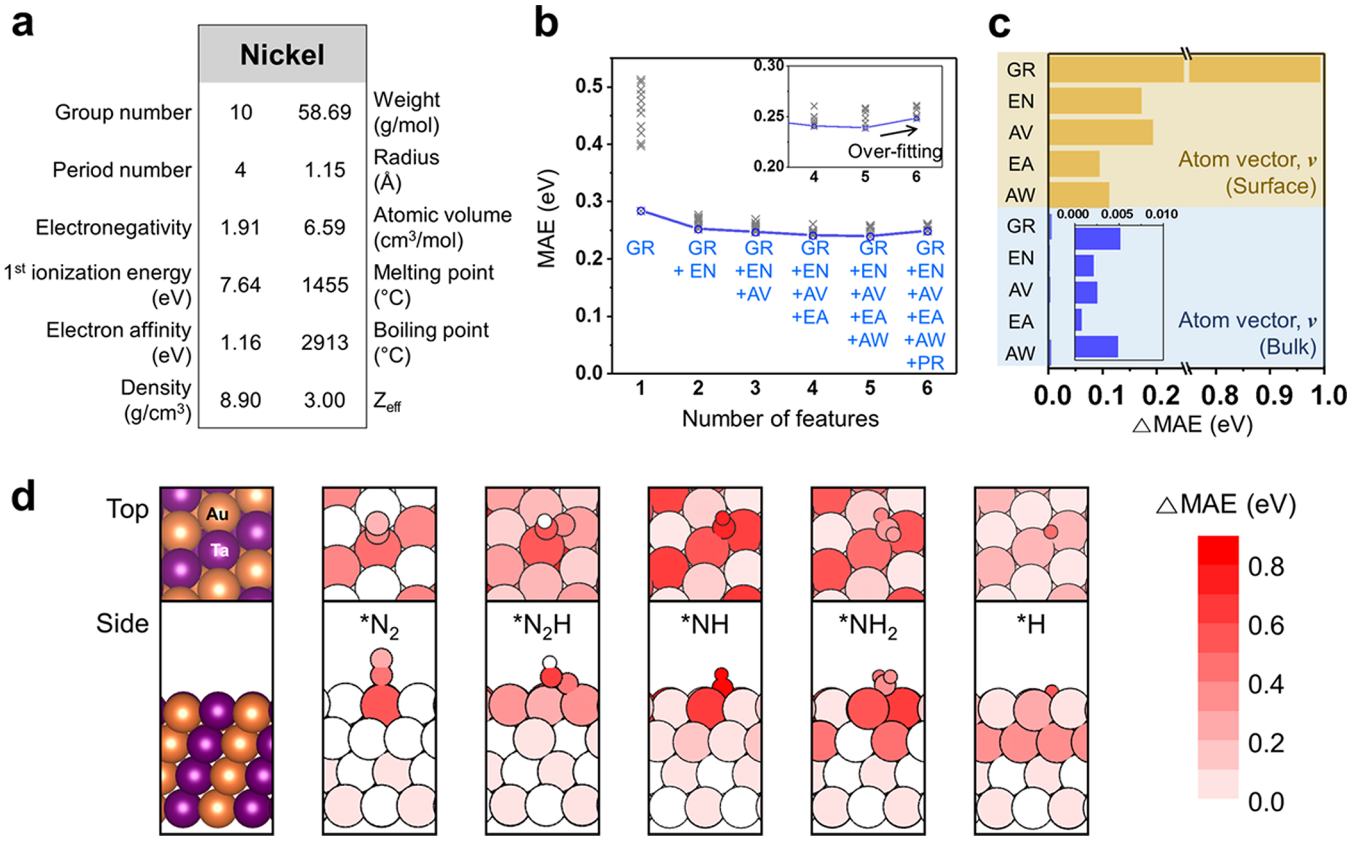

Figure 4. Feature engineering and occlusion sensitivity tests. (a) Types of atomic input features (12 elemental properties for Ni element as an example) (b) Feature optimization test. MAE values as a function of various feature combinations. Blue points/lines denote the minimum value at each feature number. (c, d) Occlusion sensitivity tests. (c) ΔMAE (the increase in MAE) as a function of occluded feature types in each bulk or surface graph. (d) Slab geometries (TaAu−$L1_0$−(111) system) with each atom colored by the magnitude of ΔMAE upon its occlusion. All five adsorbates (N_2, N_2H, NH, NH_2, and H) are considered in this test.

5%, where ε denotes the shell strain experienced due to the lattice mismatch with core elements (263 systems). For slab surface calculations, the closest-packed surfaces of each crystal structure were considered: (111) for fcc metals or $L1_0$ compounds, (110) for bcc metals or B2 compounds, and (001) for hcp metals. See the Methods section for details of the database generation and DFT calculations.

For each catalyst material, five different adsorbates (H, N_2, N_2H, NH, and NH_2) are considered because the binding energies of these adsorbates (ΔE_{ads}) are directly related to the determination of U_L or F (Figure 2c). The interaction chemistry between the catalyst surface and adsorbates varies substantially with adsorbate type, as confirmed by the ΔE_{ads} variation for each adsorbate. For *H or *N_2, for instance, ΔE_{ads} is relatively small and ranges over only ∼2 eV, in contrast to the values of the other three adsorbate cases (*N_2H, *NH, and *NH_2), for which ΔE_{ads} is generally larger in magnitude and the variations are also large, exceeding ∼6 eV. We highlight that the database (3040 data) is uniformly sampled over a wide range of chemical elements (30 elements), catalyst materials (OI and CS types), adsorbates (5 types), and binding energies (over 8 eV). Such wide and uniform sampling is critical for ML model training and test.

SGCNN Development and Performance. With the database established, we now introduce a new ML model, namely, SGCNN. SGCNN is an extended model of the crystal graph CNN (CGCNN) that is applicable to bulk solids.[38] Although CGCNN has proven its excellence in predicting several bulk properties including the bulk formation energy, band gap, and elastic constants, surface-related properties cannot be tested because the graph structure is limited to bulk solids. Hence, the model cannot be applied to catalyst systems, which involve mostly surface reactions. To solve this problem and to incorporate surface effects, we constructed two independent graphs (Figure 3a). One is a bulk graph (**B**), which is identical to the one in the CGCNN model, and the other is a surface graph ($\mathbf{S_1}$ or $\mathbf{S_2}$), which is based on adsorbates and the top ($\mathbf{S_1}$) or top two ($\mathbf{S_2}$) surface layers. In each graph, the nodes represent atoms, and the edges represent connections between atoms. Convolution layers and a pooling layer were built on top of the bulk and surface graphs. Two pooled vectors originating from the bulk and surface graphs are concatenated, and the result is related to the adsorbate binding energy via fully connected layers (FCLs). The details regarding slab graph construction, convolution functions, pooling functions, hyperparameter tuning, loss functions, regularization, and code availability are well elaborated in the Methods section.

SGCNN performs very well in predicting adsorbate binding energies, as shown in Figure 3b−d. For optimization, we tested five graphs: **B** (bulk graph), $\mathbf{S_1}$ (surface graph with top 1 layer), $\mathbf{S_2}$ (surface graph with top 2 layers), **B** + $\mathbf{S_1}$, and **B** + $\mathbf{S_2}$. Unsurprisingly, the bulk-only graph (**B**) performs very poorly (Figure 3c), as it does not incorporate surface effects. $\mathbf{S_2}$ (or **B** + $\mathbf{S_2}$) performs better than $\mathbf{S_1}$ (or **B** + $\mathbf{S_1}$), which likely indicates that both the top and subsurface layers interact with

https://dx.doi.org/10.1021/acs.chemmater.9b03686
Chem. Mater. XXXX, XXX, XXX−XXX

adsorbates. Among the five graphs, **B** + $\mathbf{S_2}$ performs the best, leading to an MAE of 0.23 eV (Figure 3d), estimated after 5-fold cross-validations, where no overfitting phenomenon occurs, as shown in Figure 3e. Previous ML models primarily developed for CO_2 reduction catalysis also report comparable MAE or root-mean-squared error (RMSE) values of approximately 0.12−0.3 eV for CO binding energy predictions.[28−30] However, it is important to note that the binding energies in our database range over 8 eV, in contrast to previous studies in which CO binding energies were reported to range over only approximately 2 eV. A detailed comparison of the prediction accuracy with that of previous models in the literature is provided in Table S2.

In Figure 3b, we report the results for different catalyst types (OI vs CS). Regardless of the graph structure, the surface−adsorbate interactions for OIs are relatively difficult for SGCNN to learn compared to those for CSs. For the **B** + $\mathbf{S_2}$ structure, for instance, the MAE determined based on the OI data is 0.34 eV, while the MAE determined based on the CS data is much smaller at 0.14 eV. The reason is that, for CS data, the adsorption energies are strongly dependent on the shell elements alone (with little dependence on the core elements), which simplifies the surface interaction chemistry. We also report the prediction accuracy by adsorbate type (H, N_2, N_2H, NH, and NH_2) in Figure 3f. The variation in MAE values is fairly small over all adsorbates: the difference between the smallest and largest MAE is less than 0.08 eV. Interestingly, the effect of the binding energy range of each adsorbate dataset (e.g., ∼2 eV for $*N_2$ and ∼6 eV for *NH) on the final MAE values is relatively weak; fairly uniform MAEs were observed for all adsorbates.

The above analysis highlights the superior flexibility of the SGCNN model. The introduction of a graph network makes SGCNN highly adapted to structural variations. SGCNN is tolerant of the diverse data resulting from different crystal spaces for catalyst materials (e.g., fcc, bcc, hcp, $L1_0$, B2, and CS-type), exposed surfaces ((111), (110), and (001)), and adsorbate types and sites (in our work, five types and up to four sites per adsorbate type). These diverse data (>3000) can simultaneously be used for the SGCNN training; as a result, a trained SGCNN with a single set of weight matrices can accurately predict the binding energies of such diverse cases (Figures 3f and S3). In contrast, other regression models that do not utilize graph networks are much less tolerant of data diversity due to their fixed architecture for the input feeding, and therefore, they are trained with only a small number of data (<250, Table S2) in a limited chemical space (in most cases, a single crystal structure and a single adsorbate).[26,28−30]

Low-Level Input Features. The level of input features used for SGCNN training is critical for the purpose of accelerated material discovery. Previous studies have used ab initio-level surface features, such as d-band characteristics (d-band center or shape) as key inputs.[28,30] These models capture the catalyst−adsorbate interactions well, likely owing to the strong correlation (d-band theory) between the d-band center and adsorption energies.[46,47] However, the use of these models for accelerated screening processes remains a challenge because they require additional DFT computations to prepare ML inputs. SGCNN can overcome this limitation since it only requires inputs of elemental properties available in the periodic table of elements and connectivity information of constituent atoms. Twelve elemental properties were considered (Figure 4a): GR, PR, Pauling scale electronegativity (EN), 1st ionization energy (IE, in eV), electron affinity (EA, in eV), density, atomic weight (AW, in g/mol), covalent radius (in Å), atomic volume (AV, in cm^3/mol), melting point (in °C), boiling point (in °C), and effective nuclear charge (Z_{eff}).[48]

Some specific partial combination of these features would lead to a minimum prediction error, and we carried out a process to identify that error. Because exploring all possible combinations ($\sum_{n=1}^{12} C_n$ = 4095 combinations) is too costly, the process was performed in a more efficient manner (Figure 4b). Out of the 12 features, the feature that yielded the smallest error when used alone (in this case, GR) was adopted first. Then, the next feature that reduced the error the most when combined with the first was added. The process was terminated when the addition of any available feature no longer reduced the error but instead caused overfitting. The best combination leading to the minimum MAE of 0.23 eV consists of only five features, i.e., GR, EN, AV, EA, and AW. The addition of any feature to this combination undermines the prediction accuracy, as overfitting occurs (inset of Figure 4b). It should be noted that model training with GR alone leads to an MAE of 0.28 eV, indicating its superior importance in predicting adsorption energies. Since the GR of an element is linearly correlated with the *d*-block electron number, it likely serves as an alternative descriptor of the *d*-band center of the catalyst material.

Key Learning Components Revealed by the Occlusion Sensitivity Test. The occlusion sensitivity test[49] is performed to quantify the importance of each feature or atom in the model training performances and thereby to extract the main components that SGCNN has learned. Figure 4c shows the increase in MAE (ΔMAE) when a specific feature of atom nodes in either the bulk or surface graph is occluded, i.e., nullified with all-zero entries. The test reveals the strong sensitivity of adsorption energies to the features of the surface graph relative to those of the bulk graph. In particular, the occlusion of the GR of constituent elements in the surface graph leads to the most severe malfunction of SGCNN, resulting in a ΔMAE of approximately 1.0 eV, compared to cases involving the other four features (ΔMAE between ∼0.1 and 0.2 eV).

With TaAu(111) as an example, an occlusion sensitivity test is carried out for each constituent atom (Figure 4d). Each atom is colored by the magnitude of ΔMAE upon its occlusion. All five adsorbates are considered in this test, and with no exception, adsorbates and their first-nearest neighbors (atoms in deep red) turn out to be particularly important in the model functioning. Even surface atoms, when not connected to the adsorbate, are found much less influential. This analysis confirms that the training process enables SGCNN to mainly learn the local environments at catalytic surfaces. Therefore, the proper construction of a surface graph (in particular, connectivity information around adsorbates) would be critical for SGCNN to learn the surface interactions and consequently to predict adsorption energies accurately.

Statistical Data Analysis. *t*-SNE analysis[50,51] was performed to group catalyst materials based on U_L values. Because the binding energies of four adsorbates (N_2, N_2H, NH, and NH_2) determine U_L, we first computed the Pearson correlation coefficient (ρ_{corr}) between the binding energy of each adsorbate and U_L and identified the NH_2 species as the most strongly correlated with ρ_{corr} = 0.73 (Figure S4). Thus, the feature vectors following the pooling process in SGCNN

https://dx.doi.org/10.1021/acs.chemmater.9b03686
Chem. Mater. XXXX, XXX, XXX−XXX

for NH_2 cases were used in *t*-SNE analysis. In Figure 5a, each site (representing each catalyst material) is colored according

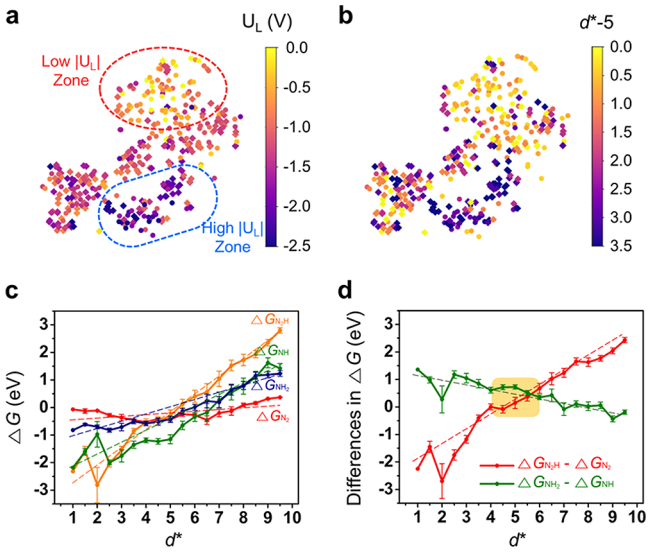

Figure 5. Statistical data analysis to reveal correlations between d^* and U_L. (a) *t*-SNE analysis of feature vectors of NH_2 adsorbate cases with the color bar representing U_L values. The *x* and *y* axes represent a reduced 2D feature space. Low $|U_L|$ and high $|U_L|$ zones are highlighted. (b) *t*-SNE analysis using the same feature vectors with the color bar representing d^*-5. (c) Average ΔG_{N_2}, ΔG_{N_2H}, ΔG_{NH}, and ΔG_{NH_2} values as a function of d^*, with the bars of standard error of the mean. The slopes of the fitted linear lines are 0.06, 0.62, 0.43, and 0.26 eV for ΔG_{N_2}, ΔG_{N_2H}, ΔG_{NH}, and ΔG_{NH_2}, respectively. (d) Average $\Delta G_{N_2H}-\Delta G_{N_2}$ or $\Delta G_{NH_2}-\Delta G_{NH}$ values as a function of d^*, with the bars of standard error of the mean. The yellow shade highlights the region of $4 \le d^* \le 6$, where materials requiring small limiting potentials are the most likely to be discovered.

to its U_L value. The low $|U_L|$ (<1.0 eV) vs high $|U_L|$ (>2.0 eV) regions are clearly separated in space and distinguished by color (yellow vs blue). The low $|U_L|$ region consists mostly of OI-type materials (●) rather than CS-type materials (◆). This finding implies that some binary OI compounds may overcome the known linear relations (the line in Figure 1b) and potentially lie in the promising U_L zone, whereas most CS-type materials are unlikely to do so. This difference is likely because the exposed surfaces of CS-type alloys are identical to pure metal cases, and the strain effect (due to core and shell lattice mismatch) is minor; thus, the performance of CS-type alloys does not deviate from the pure metal regime. In contrast, intermetallics have mixed elements on the exposed surface, likely causing energetics that are not observed for pure metals.

Another *t*-SNE analysis (Figure 5b) was performed using the same feature vectors in Figure 5a, with each site colored by d^*-5, where d^* is the average d-orbital occupation of the top surface layer: $d^* = (d_A + d_B)/2$ for OIs and d_{shell} for CS materials, where d_X is the d-block electron number of the element X. The *t*-SNE results in Figure 5a,b show high similarity between the color distributions, leading to a statistical inference that low $|U_L|$ materials mostly exhibit d^* values between 4 and 6. For binary OIs such as $L1_0$ and B2 crystals to satisfy $4 \le d^* \le 6$, one element should be an early transition metal (ETM; GRs 3−5 in Figure 2a) and the other element, a late transition metal (LTM; GRs 7−11 in Figure 2a). Indeed, the catalyst materials in our database requiring smaller limiting potential than Mo(110) consist mostly of one ETM and the other LTM so that d^* lies between 4 and 6.

To quantitatively understand the relationship between d^* and U_L, the trend of binding energies of each adsorbate (ΔG_{N_2}, ΔG_{N_2H}, ΔG_{NH}, and ΔG_{NH_2}) with d^* is analyzed in Figure 5c. All adsorbates tend to bind to catalyst surfaces more strongly with decreasing d^* (or increasing *d*-band center, Figure S5); however, it should be noted that the sensitivity, estimated by the slope of each fitted line, differs substantially by adsorbate types. For instance, the slope for the N_2 case is ∼0.06 eV and that for N_2H is ∼0.62 eV, indicating much stronger sensitivity of ΔG_{N_2H} to d^* than ΔG_{N_2}. In Figure 5d, the differences in ΔG ($\Delta G_{N_2H}-\Delta G_{N_2}$ or $\Delta G_{NH_2}-\Delta G_{NH}$), the maximum of which determines U_L, are shown with d^* variations. Because of the aforementioned slope differences, $\Delta G_{N_2H}-\Delta G_{N_2}$ increases with d^*, whereas $\Delta G_{NH_2}-\Delta G_{NH}$ decreases with d^*, and these two curves cross over at around $d^* = 5.5$. This quantitative analysis adequately explains why materials requiring small limiting potentials are mostly discovered in the region of $4 \le d^* \le 6$ (quasi-plateau of U_L) and further supports d^* as a simple orbital-occupation guideline to lower the limiting potential in the NRR.

SGCNN-Driven Prediction of Novel Catalyst Candidates. We now utilize the trained SGCNN model to accelerate the discovery of novel catalysts that were not parts of our training database. The target crystal space is $L1_2$ ordered structures (A_3B) with the constituent elements (A and B) in PRs 4−6 and GRs 3−13, as shown in Figure 2a. The closest-packed (111) surfaces of a total of 870 ($_{30}P_2$) candidate catalysts were chosen for tests (Figure 6a).

A fully ML-driven screening process (Figure 6b) is performed based on the following three criteria: (i) stability, estimated by E_f; (ii) limiting potential; and (iii) Faradaic efficiency, estimated by *F*. For E_f prediction, we use the original CGCNN model.[38] CGCNN has proven its excellence in predicting E_f with a very small MAE of 0.039 eV/atom for 28 046 bulk structures in the Materials Project database.[52] Out of a total of 870 candidates, 364 materials with negative E_f are screened first and considered in the subsequent processes. The latter two steps are based on the SGCNN predictions of the adsorption energies of H, N_2, N_2H, NH, and NH_2 species. The next criterion is a lower limiting potential than Mo(110), i.e., $|U_L| < 0.92 + T$ (V), where *T* (tolerance) is 0.23, which is adopted from the MAE value of the pretrained SGCNN model. Note that *T* is included in the screening criterion to complement the inevitable error in ML predictions. The last criterion is $F < -0.18 + T$ (eV), toward an improved Faradaic efficiency relative to Mo(110). As shown in Figure 6c, only 10 materials finally remained and deserve DFT verification along an entire NRR pathway and future experimentations. Overall, the SGCNN-based screening process substantially narrows down the search space from a total of 870 to only 10 surfaces. A full list of 10 screened materials is available in Table S3.

DFT Verification of Full NRR Paths for Promising Catalysts. DFT calculations are performed for the 10 screened materials to confirm that the ML predictions are reliable even in the $L1_2$ crystal space. First, we compare the E_f values for their bulk phases predicted by CGCNN vs DFT models, as summarized in Table S3. The MAE value is less than 0.05 eV/atom, similar to the reported accuracy (∼0.04

https://dx.doi.org/10.1021/acs.chemmater.9b03686
Chem. Mater. XXXX, XXX, XXX−XXX

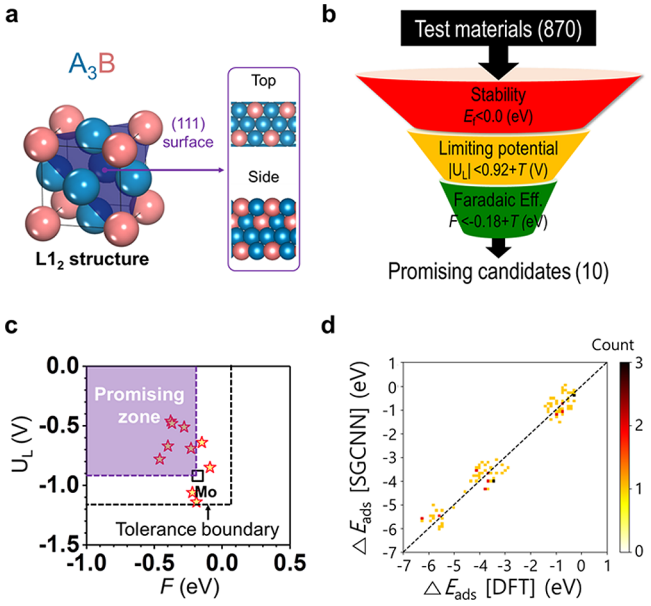

Figure 6. ML-driven predictions and DFT verification to identify novel catalysts in the $L1_2$ crystal space. (a) Schematic describing bulk and (111) surface structures of the $L1_2$ ordered phase (A_3B). (b) Fully ML-driven screening process to search for stable and efficient catalysts that potentially outperform Mo(110) in the NRR. T (tolerance) is 0.23, which is adopted from the MAE value of the pretrained SGCNN model. (c) U_L and F values predicted by the SGCNN model for the 10 screened materials. DFT-computed U_L and F values of Mo(110) are shown as a reference to define the promising zone and tolerance boundary. (d) 2D histogram comparing the predicted adsorption energies using the SGCNN model and DFT computations for the 10 screened materials.

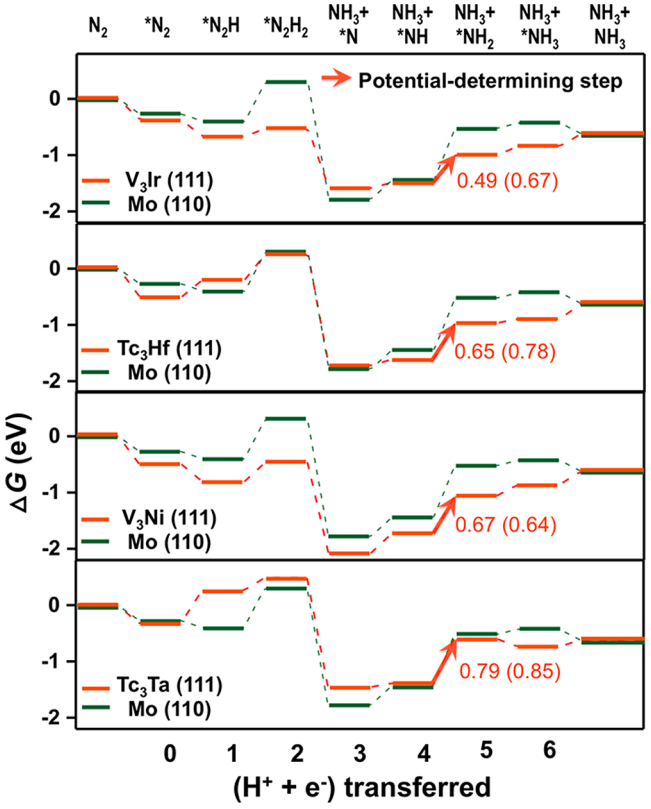

Figure 7. DFT-computed free energy diagrams along the full NRR path of four proposed catalysts, in comparison to those of Mo(110). PDSs are highlighted with arrows. Materials are listed in the order of low to high $|U_L|$ values (DFT predictions). Numbers in the parentheses denote $|U_L|$ values predicted by the SGCNN model, for comparisons.

eV/atom) of the original work.[38] Second, Figure 6d compares the adsorption energies (H, N_2, N_2H, NH, and NH_2) between the SGCNN and DFT predictions, and the MAE value is found to be 0.35 eV. This value is approximately 0.1 eV larger than the MAE (0.23 eV) from the model development stage. Although slightly increased, the prediction error in the $L1_2$ space is still small enough to substantially improve the efficiency of the NRR catalyst search.

The entire NRR pathway for these materials is investigated by DFT computations, which show that four of the 10 materials indeed perform better than the reference Mo(110) in terms of both criteria of $|U_L| < 0.92$ V and $F < -0.18$ eV. These four are listed below from low to high $|U_L|$: V_3Ir ($|U_L| = 0.49$ V; $F = -0.22$ eV), Tc_3Hf ($|U_L| = 0.65$ V; $F = -0.28$ eV), V_3Ni ($|U_L| = 0.67$ V; $F = -0.37$ eV), and Tc_3Ta ($|U_L| = 0.79$ V; $F = -0.23$ eV). The free energy diagrams along the full NRR path for these four materials are shown in Figure 7, in comparison to the reference Mo(110). The DFT-verified energetics of negative E_f, low limiting potential (as small as 0.49 V), and low F (as small as −0.37 eV) warrant immediate experimental evaluations of the NRR performance of these materials.

Revisiting the d^* criterion in Figure 5, we observe that it is still valid even for $L1_2$ materials (A_3B), where d^* is defined as $(3d_A + d_B)/4$. All four candidates requiring smaller limiting potentials than Mo(110) exhibit d^* between 4.0 and 4.5, as follows: $d^* = 4.0$ (V_3Ir), 4.25 (Tc_3Hf, V_3Ni), and 4.5 (Tc_3Ta). This analysis of $L1_2$ materials is consistent with the results in Figure 5d that materials with $4 \leq d^* \leq 6$ may potentially overcome the scaling relation observed in Figure 1b; it further supports d^* as a useful orbital-occupation guideline for NRR catalyst design.

We note that three following points are noticeable and should be discussed. First, for the newly screened materials, the rank (e.g., in terms of U_L) between SGCNN and DFT prediction is not the same as shown in Table S3, and this difference is inevitable due to the ML prediction error (MAE of 0.23 eV). However, we emphasize that the main value of our ML model is to narrow down the search space (in this case, 870 → 10) and dramatically enhance the search efficiency. Second, we note that PDSs for these four catalysts are all found at *NH → $*NH_2$, which is consistent with the assumption that energetics of $*N_2$ → $*N_2H$ vs *NH → $*NH_2$ mainly compete for PDS and U_L determination in the NRR. Lastly, we also note in Figure S1 that, for the new catalysts, the distal pathway offers lower U_L values relative to alternating and enzymatic ones, which does not violate our initial assumption that the distal mechanism is dominant in flat slab models.

We would like to discuss about the expansion of our model to ternary compounds, although only the $L1_2$ crystal space was studied for new catalyst discovery in this work. We further studied ternary compounds, in particular alloy-core@shell structures, which have recently been studied for CO oxidation reaction.[53] This material is overall in core−shell architecture, while the core part is ordered intermetallics; thus, it is expected to be in a similar data distribution with our ML training space. As a result of tests for three random alloy-core@shell structures (ReOs@Rh, PdPt@Ru, and PdPt@Ir), we find

https://dx.doi.org/10.1021/acs.chemmater.9b03686
Chem. Mater. XXXX, XXX, XXX−XXX

that SGCNN well predicts the binding energies of all five adsorbates with the MAE of only 0.13 eV, indicating that our model can be effectively expanded to ternary compounds. The detailed results of SGCNN predictions for alloy-core@shell structures are available in Figure S6.

CONCLUSIONS

Overall, we developed a machine learning model (SGCNN) that learns surface interactions in NRR catalysis. With a self-accumulated database of 3040 surface DFT calculations, SGCNN predicted the binding energies, ranging over 8 eV, of five adsorbates (H, N_2, N_2H, NH, and NH_2) that are directly related to NRR performance with an MAE of only 0.23 eV. SGCNN only requires the low-dimensional inputs of elemental properties available in the periodic table of elements and connectivity information of constituent atoms. As a result, the model is suited for an accelerated screening process. Via a combined process of SGCNN-driven predictions over the $L1_2$ crystal space and DFT verification, four novel catalysts in the $L1_2$ crystal space, i.e., $V_3Ir(111)$, $Tc_3Hf(111)$, $V_3Ni(111)$, and $Tc_3Ta(111)$, are proposed as stable candidates that outperform the reference Mo(110) in terms of both the U_L and F criteria; immediate experimental evaluation of their NRR performance is warranted. The SGCNN-based screening process, which prioritizes the unexplored materials in terms of E_f, U_L, and F, can significantly narrow down the search space, which enables accelerations of the novel catalyst discovery. A t-SNE analysis further suggests that catalytic surfaces with d^* values between 4 and 6 may potentially lower the limiting potential in the NRR, providing an insightful guideline for orbital occupations to improve catalytic performance.

METHODS

DFT Calculations for Adsorption Energy Data Accumulation. Spin-polarized DFT calculations were performed using the Vienna Ab initio Simulation Package (VASP) with projector-augmented-wave pseudopotentials[54,55] and the revised Perdew–Burke–Ernzerhof (RPBE)[56] exchange–correlation functional. Grimme's DFT–D3 method[57] was adopted to treat van der Waals interactions for the improved description of adsorption energy.[43,58,59] Note that the Hubbard U term is not implemented in this work. Although the inclusion of the Hubbard U term is important for metal oxide catalyst systems where d states are strongly localized,[60−62] the U term little affects the adsorption energy by less than 0.05 eV in pure metal systems (materials investigated in the current study), where electronic states are delocalized. See Table S4 for the effect of Hubbard U terms. A plane-wave kinetic energy cutoff of 520 eV was used. For k-point sampling, an 8 × 8 × 8 Monkhorst–Pack mesh was used for bulk systems, while a 6 × 6 × 1 Monkhorst–Pack mesh was used for slab systems.[63] The slab of a 2 × 2 unit cell consists of four layers. The bottom two layers were fixed, and the top two layers and adsorbates were fully relaxed until the forces acting on the individual atoms were less than 0.05 eV/Å. A vacuum spacing of 15 Å (in the z-direction) was used to prevent spurious interactions between slabs. Various adsorbate positions on slabs were considered: (1) N_2 adsorbates were placed vertically on the slab at top sites; (2) N_2H, NH, and NH_2 adsorbates were placed horizontally on the slab at top, hollow, and bridge sites; and (3) H adsorbates were placed on the slab at top and hollow sites. The details of the adsorption geometries are summarized in Figure S7. The adsorbate binding energies were calculated by the following equation: $\Delta E_{ads} = E[\text{slab + ads.}] - E[\text{slab}] - E[\text{ads.}]$, where E[slab + ads.], E[slab], and E[ads.] are the total energies of the slab+adsorbate, slab-only, and adsorbate-only configurations. During SGCNN training, E[ads.] of N_2H, NH, and NH_2 molecules were not referenced to N_2 or H_2 gas states but referenced to each radical itself so that binding energies of each adsorbate span over different ranges. Training with the radical referencing improves the MAE by approximately 0.1 eV, relative to the other case using N_2 and H_2 gas states as the reference.

Free Energy Corrections. The free energies of adsorbates were estimated under standard reaction conditions (pH = 0; T = 298 K; P = 1 atm) at a potential of U = 0. The chemical potential of $(H^+ + e^-)$ was estimated to be equal to that of $0.5H_2$. The thermochemical free energy is given by $\Delta G_{ads} = \Delta E_{ads} + \Delta G_{corr}$, where ΔG_{corr} denotes free energy correction.[44] Importantly, note that ΔE_{ads} was referenced to N_2 and H_2 gas for ΔG_{ads} estimations. The ΔG_{corr} values were estimated using a standard vibrational correction in the harmonic approximation to enthalpy and entropy as follows: $\Delta G_{corr} = \Delta E_{ZPE} + \Delta H_{corr} - T\Delta S_{corr}$, where ΔE_{ZPE}, ΔH_{corr}, and $T\Delta S_{corr}$ are the zero-point energy correction, enthalpy correction, and entropy correction terms, respectively, and the values for each adsorbate are available in Table S1. Solvation effects were ignored because the solvation-induced stabilization energy of adsorbates in the NRR is less than 0.1 eV.[43]

Slab Graph Constructions. Graphs are mathematical representations of system structures, where nodes and edges correspond to atoms and bonds, respectively. Multiple edges are allowed to represent the periodicity of solids. SGCNN consists of two independent graphs: a bulk graph ($\mathbf{B}$) and a surface graph ($\mathbf{S_1}$ or $\mathbf{S_2}$), as depicted in Figure 3a. The surface graph captures the catalyst–adsorbate interactions by characterizing adsorbate types and adsorption sites. Each ith atom (node) in a system is encoded into an atom vector v_i, which is based on the elemental properties that are readily available from the periodic table of elements. Atomic features are encoded in a one-hot manner due to their categorical property. A list of atomic input features and their ranges/units/categories is available in Table S5. Each bond (edge) between the ith and jth atoms is defined only if $d_{(i,j)} < r_i + r_j + \Delta$, where $d_{(i,j)}$ is the distance between the ith and jth atoms, and r_i and r_j denote the covalent radii of each atom, with the tolerance Δ being 1.5 Å. Each bond is encoded into a bond vector, i.e., $u_{(i,j)_k} = 1$, where k is the kth edge connecting the center node i and neighbor j. Note that we intentionally set the bond vector as distance-insensitive, unlike the original CGCNN work.[38] As a result, the connectivity information required as an ML input is whether or not arbitrary atom pairs are connected (yes or no question), instead of their distance values.

Convolution and Pooling Functions. CNN processes are performed on top of each bulk and surface graph, which consists of a sequence of convolutions, pooling, and FCLs. The convolution functions first concatenate neighbor vectors $z_{(i,j)_k}^{(t,f)} = v_i^{(t,f)} \oplus v_j^{(t,f)} \oplus u_{(i,j)k}$ and then perform convolutions to update each atom vector, as follows:

$$v_i^{(t+1,f)} = v_i^{(t,f)} + \sum_{j,k} \sigma(z_{(i,j)_k}^{(t,f)} W_1^{(t,f)} + b_1^{(t,f)}) \odot g(z_{(i,j)_k}^{(t,f)} W_2^{(t,f)} + b_2^{(t,f)})$$

where t and f parameters denote the numbers of convolutional layer and filter, respectively, $\oplus$ denotes concatenation, $\odot$ denotes element-wise multiplication, σ is a sigmoid function, g is the exponential linear unit (ELU) activation function, and $W_1^{(t,f)}$, $W_2^{(t,f)}$ and $b_1^{(t,f)}$, $b_2^{(t,f)}$ are convolution weight matrices and biases of the tth layer and fth filter, respectively.[38,64] The effect of the number of convolution layers and filters on the prediction accuracy is shown in Figure S8. The pooling function is selected as the normalized summation of all atom vectors (after R convolutions), i.e., $v_{pool} = \sum_{i,f} v_i^{(R,f)}$. The final feature vector resulting from the pooling process is extracted in the same dimension as each atom vector. Two pooled vectors originating from each bulk and surface graph are concatenated, and the result is finally related to the adsorbate binding energy via the FCLs.

Hyperparameter Tuning, Loss Function, and Regularization. The following hyperparameters are tested, and the optimized values are shown in parentheses: the number of convolution filters and layers (1 filter, 3 layers), learning rate (5×10^{-3}), exponentially decaying learning rate (0.97 for every 100 epochs), nodes of the FCLs (3 layers with 10 → 2 → 1 nodes/layer), standard deviation of

https://dx.doi.org/10.1021/acs.chemmater.9b03686
Chem. Mater. XXXX, XXX, XXX−XXX

normally distributed random initial weights (0.1), batch size (64), and total number of epochs (1000). The loss function $J(\mathbf{y}, \hat{\mathbf{y}}(\boldsymbol{W}))$ is set as the mean squared error (MSE). During the training phase, the loss function J is minimized using the Adam optimization algorithm.[65] Two regularization techniques are used to reduce overfitting: dropout[66] and $\mathbf{L}^2$ weight decay. For dropout, we randomly disconnect some neurons during the training phase with a dropout probability and restore the complete network with proper scaling in the test phases. The optimized dropout probability and $\mathbf{L}^2$ regularization coefficients are 0.2 and 10^{-2}, respectively. A list of hyperparameters and their ranges for the optimization process is available in Table S6.

SGCNN Training Time and Code Availability. The proposed SGCNN is implemented in Python (version 3.5) using the TensorFlow framework (version 1.7.0). The training time required is approximately half an hour to obtain 5-fold cross-validation results for each SGCNN network using GeForce GTX 1080 Ti GPU. The SGCNN implementation code is available at https://github.com/myungjoon/SGCNN.

■ ASSOCIATED CONTENT

Supporting Information

The Supporting Information is available free of charge at https://pubs.acs.org/doi/10.1021/acs.chemmater.9b03686.

Free energy diagrams for various metals or NRR pathways (Figures S1 and S2), free energy correction terms (Table S1), details of SGCNN model performances (Table S2 and Figure S3), statistical analysis relating d^* and U_L (Figures S4 and S5), ML tests for $L1_2$ and ternary compounds (Table S3 and Figure S6), comparisons of DFT functionals (Table S4), possible surface configurations for adsorbates (Figure S7), details of ML inputs and hyperparameters (Tables S5 and S6, Figure S8) (PDF)

■ AUTHOR INFORMATION

Corresponding Authors

Sang Soo Han − *Korea Institute of Science and Technology, Seoul, Republic of Korea;* orcid.org/0000-0002-7925-8105; Email: sangsoo@kist.re.kr

Donghun Kim − *Korea Institute of Science and Technology, Seoul, Republic of Korea;* orcid.org/0000-0003-0326-5381; Email: donghun@kist.re.kr

Other Authors

Myungjoon Kim − *Korea Institute of Science and Technology, Seoul, Republic of Korea*

Byung Chul Yeo − *Korea Institute of Science and Technology, Seoul, Republic of Korea*

Youngtae Park − *Korea Advanced Institute of Science and Technology, Daejeon, Republic of Korea*

Hyuck Mo Lee − *Korea Advanced Institute of Science and Technology, Daejeon, Republic of Korea;* orcid.org/0000-0003-4556-6692

Complete contact information is available at: https://pubs.acs.org/10.1021/acs.chemmater.9b03686

Author Contributions

§M.K. and B.C.Y. contributed equally to this work.

Notes

The authors declare no competing financial interest.

■ ACKNOWLEDGMENTS

This work was supported by Creative Materials Discovery Program through the National Research Foundation of Korea (NRF-2016M3D1A1021140) and Samsung Research Funding & Incubation Center of Samsung Electronics (Project no. SRFC-MA1801-03).

■ REFERENCES

(1) Erisman, J. W.; Sutton, M. A.; Galloway, J.; Klimont, Z.; Winiwarter, W. How a century of ammonia synthesis changed the world. *Nat. Geosci.* **2008**, *1*, 636.

(2) Smil, V. *Enriching the Earth: Fritz Haber, Carl Bosch, and the Transformation of World Food Production*; MIT Press: Cambridge, MA, 2004.

(3) Jennings, J. R. *Catalytic Ammonia Synthesis: Fundamentals and Practice*; Springer Science & Business Media: New York, 2013.

(4) Foster, S. L.; Perez Bakovic, S. I.; Duda, R. D.; Maheshwari, S.; Milton, R. D.; Minteer, S. D.; Janik, M. J.; Renner, J. N.; Greenlee, L. F. Catalysts for nitrogen reduction to ammonia. *Nat. Catal.* **2018**, *1*, 490−500.

(5) Renner, J. N.; Greenlee, L. F.; Ayres, K. E.; Herring, A. M. Electrochemical synthesis of ammonia: A low pressure, low temperature approach. *Electrochem. Soc. Interface* **2015**, *24*, 51−57.

(6) Shipman, M. A.; Symes, M. D. Recent progress towards the electrosynthesis of ammonia from sustainable resources. *Catal. Today* **2017**, *286*, 57−68.

(7) Kyriakou, V.; Garagounis, I.; Vasileiou, E.; Vourros, A.; Stoukides, M. Progress in the electrochemical synthesis of ammonia. *Catal. Today* **2017**, *286*, 2−13.

(8) Guo, C.; Ran, J.; Vasileff, A.; Qiao, S. Z. Rational design of electrocatalysts and photo(electro)catalysts for nitrogen reduction to ammonia (NH_3) under ambient conditions. *Energy Environ. Sci.* **2018**, *11*, 45−56.

(9) Kordali, V.; Kyriacou, G.; Lambrou, C. Electrochemical synthesis of ammonia at atmospheric pressure and low temperature in a solid polymer electrolyte cell. *Chem. Commun.* **2000**, *17*, 1673.

(10) Geng, Z.; Liu, Y.; Kong, X.; Li, P.; Li, K.; Liu, Z.; Du, J.; Shu, M.; Si, R.; Zeng, J. Achieving a record-high yield rate of 120.9 ugNH3 mg-1 h-1 for N2 electrochemical reduction over Ru single-atom catalysts. *Adv. Mater.* **2018**, *30*, No. 1803498.

(11) Licht, S.; Cui, B. C.; Wang, B. H.; Li, F.-F.; Lau, J.; Liu, S. Z. Ammonia synthesis by N_2 and steam electrolysis in molten hydroxide suspensions of nanoscle Fe_2O_3. *Science* **2014**, *345*, 637−640.

(12) Chen, S.; Perathoner, S.; Ampelli, C.; Mebrahtu, C.; Su, D.; Centi, G. Electrocatalytic synthesis of ammonia at room temperature and atmospheric pressure from water and nitrogen on a carbon-nanotube-based electrocatalyst. *Angew. Chem., Int. Ed.* **2017**, *56*, 2699.

(13) Li, S.-J.; Bao, D.; Shi, M.-M.; Wulan, B.-R.; Yan, J.-M.; Jiang, Q. Amorphizing of Au nanoparticles by CeO_x-RGO hybrid support towards highly efficient electrocatalyst for N_2 reduction under ambient conditions. *Adv. Mater.* **2017**, *29*, No. 1700001.

(14) Bao, D.; Zhang, Q.; Meng, F.-L.; Zhong, H.-X.; Shi, M.-M.; Zhang, Y.; Yan, J.-M.; Jiang, Q.; Zhang, X.-B. Electrochemical reduction of N_2 under ambient conditions for artificial N_2 fixation and renewable energy storage using N_2/NH_3 cycle. *Adv. Mater.* **2017**, *29*, No. 1604799.

(15) Shi, M.-M.; Bao, D.; Wulan, B.-R.; Li, Y.-H.; Zhang, Y.-F.; Yan, J.-M.; Jiang, Q. Au sub-nanoclusters on TiO_2 toward highly efficient and selective electrocatalyst for N_2 conversion to NH_3 at ambient conditions. *Adv. Mater.* **2017**, *29*, No. 1606550.

(16) Song, Y.; Johnson, D.; Peng, R.; Hensley, D. K.; Bonnesen, P. V.; Liang, L.; Huang, J.; Yang, F.; Zhang, F.; Qiao, R.; Baddorf, A. P.; Tschaplinski, T. J.; Engle, N. L.; Hatzell, M. C.; Wu, Z.; Cullen, D. A.; Meyer, H. M., III; Sumpter, B. G.; Rondinon, A. J. A physical catalyst for the electrolysis of nitrogen to ammonia. *Sci. Adv.* **2018**, *4*, No. e1700336.

(17) Liu, Y.; Su, Y.; Quan, X.; Fan, X.; Chen, S.; Yu, H.; Zhao, H.; Zhang, Y.; Zhao, J. Facile ammonia synthesis from electrocatalytic N_2

reduction under ambient conditions on N-doped porous carbon. *ACS Catal.* **2018**, *8*, 1186.
(18) Li, Q.; He, L.; Sun, C.; Zhang, X. Computational study of MoN_2 monolayer as electrochemical catalysts for nitrogen reduction. *J. Phys. Chem. C* **2017**, *121*, 27563−27568.
(19) Zhao, J.; Chen, Z. Single Mo atom supported on defective boron nitride monolayer as efficient electrocatalyst for nitrogen fixation: A computational study. *J. Am. Chem. Soc.* **2017**, *139*, 12480−12487.
(20) Lindley, B. M.; Appel, A. M.; Krogh-Jespersen, K.; Mayer, J. M.; Miller, A. J. M. Evaluating the thermodynamics of electrocatalytic N_2 reduction in acetonitrile. *ACS Energy Lett.* **2016**, *1*, 698−704.
(21) Matson, B. D.; Peters, J. C. Fe-mediated HER vs N_2RR: Exploring factors that contribute to selectivity in $P_3^EFe(N_2)$ (E = B,Si,C) catalyst model systems. *ACS Catal.* **2018**, *8*, 1448−1455.
(22) Choi, C.; Back, S.; Kim, N. Y.; Lim, J.; Kim, Y. H.; Jung, Y. Suppression of hydrogen evolution reaction in electrochemical N_2 reduction using single-atom catalysts: A computational guideline. *ACS Catal.* **2018**, *8*, 7517−7525.
(23) Suryanto, B. H. R.; Kang, C. S. M.; Wang, D.; Xia, C.; Zhou, F.; Azofra, L. M.; Cavallo, L.; Zhang, X.; MacFarlane, D. R. Rational electrode-electrolyte design for efficient ammonia electrosynthesis under ambient conditions. *ACS Energy Lett.* **2018**, *3*, 1219−1224.
(24) Tran, K.; Ulissi, Z. W. Active learning across intermetallics to guide discovery of electrocatalysts for CO_2 reduction and H_2 evolution. *Nat. Catal.* **2018**, *1*, 696−703.
(25) Panapitiya, G.; Avendano-Franco, G.; Ren, P.; Wen, X.; Li, Y.; Lewis, J. P. Machine-learning prediction of CO adsorption in thiolated, Ag-alloyed Au nanoclusters. *J. Am. Chem. Soc.* **2018**, *140*, 17508−17514.
(26) Noh, J.; Back, S.; Kim, J.; Jung, Y. Active learning with non-*ab* initio input features toward efficient CO_2 reduction catalysts. *Chem. Sci.* **2018**, *9*, 5152−5159.
(27) Meyer, B.; Sawatlon, B.; Heinen, S.; Lilienfeld, O. A. v.; Corminboeuf, C. Machine learning meets volcano plots: computational discovery of cross-coupling catalysts. *Chem. Sci.* **2018**, *9*, 7069.
(28) Ma, X.; Li, Z.; Achenie, E. K.; Xin, H. Machine-learning-augmented chemisorption model for CO_2 electroreduction catalyst screening. *J. Phys. Chem. Lett.* **2015**, *6*, 3528−3533.
(29) Toyao, T.; Suzuki, K.; Kikuchi, S.; Takakusagi, S.; Shimizu, K.-i.; Takigawa, I. Toward effective utilization of methane: machine learning prediction of adsorption energies on metal alloys. *J. Phys. Chem. C* **2018**, *122*, 8315−8326.
(30) Gasper, R.; Shi, H.; Ramasubramaniam, A. Adsorption of CO on low-energy, low-symmetry Pt nanoparticles: energy decomposition analysis and prediction via machine-learning models. *J. Phys. Chem. C* **2017**, *121*, 5612−5619.
(31) Kitchin, J. R. Machine learning in catalysis. *Nat. Catal.* **2018**, *1*, 230−232.
(32) Jinnouchi, R.; Asahi, R. Predicting catalytic activity of nanoparticles by a DFT-aided machine-learning algorithm. *J. Phys. Chem. Lett.* **2017**, *8*, 4279−4283.
(33) Ulissi, Z. W.; Medford, A. J.; Bligaard, T.; Norskov, J. K. To address surface reaction network complexity using scaling relations machine learning and DFT calculations. *Nat. Commun.* **2017**, *8*, No. 14621.
(34) Duvenaud, D.; Maclaurin, D.; Aguilera-Iparraguirre, J.; Gomez-Bombarelli, R.; Hirzel, T.; Aspuru-Guzik, A.; Adams, R. P. Convolutional network on graphs for learning molecular fingerprints. In Proceedings of the Advances in Neural Information Processing Systems, Vol. 28, 2015; pp 2224−2232.
(35) Schütt Kristof, T.; Arbabzadah, F.; Chmiela, S.; Muller, K. R.; Tkatchenko, A. Quantum-chemical insights from deep tensor neural network. *Nat. Commun.* **2017**, *8*, No. 13890.
(36) Zeng, M.; Kumar, J. N.; Zeng, Z. et al. Graph convolutional neural network for polymer property prediction, arXiv:1811.06231. arXiv.org e-Print archive. https://arxiv.org/abs/1811.06231 (accessed Dec 27, 2019).
(37) Torng, W.; Altman, R. B. Graph convolutional neural network for predicting drug-target interactions. *J. Chem. Inf. Model.* **2019**, *59*, 4131−4149.
(38) Xie, T.; Grossman, J. C. Crystal graph convolutional neural network for accurate and interpretable prediction of material properties. *Phys. Rev. Lett.* **2018**, *120*, No. 145301.
(39) Ahmad, Z.; Xie, T.; Maheshwari, C.; Grossman, J. C.; Viswanathan, V. Machine learning enabled computational screening of inorganic solid electrolytes for suppression of dendrite formation in lithium metal anodes. *ACS Cent. Sci.* **2018**, *4*, 996−1006.
(40) Isayev, O.; Oses, C.; Toher, C.; Gossett, E.; Curtarolo, S.; Tropsha, A. Universal fragment descriptor for predicting properties of inorganic crystals. *Nat. Commun.* **2017**, *8*, No. 15679.
(41) Liu, C.; Li, Q.; Zhang, J.; Jin, Y.; MacFarlane, D. R.; Sun, C. Conversion of dinitrogen to ammonia on Ru atom supported on boron sheets: A DFT study. *J. Mater. Chem. A* **2019**, *7*, 4771−4776.
(42) Ling, C.; Niu, X.; Li, Q.; Du, A.; Wang, J. Metal-free single atom catalyst for N_2 fixation driven by visible light. *J. Am. Chem. Soc.* **2018**, *140*, 14161−14168.
(43) Montoya, J. H.; Tsai, C.; Vojvodic, A.; Norskov, J. K. The challenge of electrochemical ammonia synthesis: a new perspective on the role of nitrogen scaling relations. *ChemSusChem* **2015**, *8*, 2180−2186.
(44) Skúlason, E.; Bligaard, T.; Gudmundsdottir, S.; Studt, F.; Rossmeisl, J.; Abild-Pedersen, F.; Vegge, T.; Jonsson, H.; Norskov, J. K. A theoretical evaluation of possible transition metal electro-catalysts for N_2 reduction. *Phys. Chem. Chem. Phys.* **2012**, *14*, 1235−1245.
(45) Yeo, B. C.; Kong, J.; Kim, D.; Goddard, W. A.; Park, H. S.; Han, S. S. Electronic Structural Origin of the Catalytic Activity Trend of Transition Metals for Electrochemical Nitrogen Reduction. *J. Phys. Chem. C* **2019**, *123*, 31026−31031.
(46) Nørskov, J. K. Electronic factors in catalysis. *Prog. Surf. Sci.* **1991**, *38*, 103−144.
(47) Hammer, B.; Norskov, J. K. Why gold is the noblest of all metals. *Nature* **1995**, *376*, 2238−2240.
(48) Dynamic Periodic Table. https://ptable.com (accessed Dec 7, 2018).
(49) Zeiler, M. D.; Fergus, R. Visualizing and understanding convolutional networks. In European Conference on Computer Vision (ECCV), 2014; pp 818−833.
(50) van der Maaten, L.; Hinton, G. Visualizing data using t-SNE. *J. Mach. Learn. Res.* **2008**, *9*, 2579−2605.
(51) Xie, T.; Grossman, J. C. Hierachical visualization of materials space with graph convolutional neural networks. *J. Chem. Phys.* **2018**, *149*, No. 174111.
(52) Jain, A.; Ong, S. P.; Hautier, G.; Chen, W.; Richards, W. D.; Dacek, S.; Cholia, S.; Gunter, D.; Skinner, D.; Ceder, G.; Persson, K. A. Commentary: The Materials Project: A materials genome approach to accelerating materials innovation. *APL Mater.* **2013**, *1*, No. 011002.
(53) Zhang, L.; Henkelman, G. Computational design of alloy-core@shell metal nanoparticle catalysts. *ACS Catal.* **2015**, *5*, 655−660.
(54) Kresse, G.; Joubert, D. From Ultrasoft Pseudopotentials to the Projector Augmented-Wave Method. *Phys. Rev. B* **1999**, *59*, 1758−1775.
(55) Blochl, P. E. Projector Augmented-Wave Method. *Phys. Rev. B* **1994**, *50*, No. 17953.
(56) Hammer, B.; Hansen, L. B.; Nørskov, J. K. Improved Adsorption Energetics within Density-Functional Theory Using Revised Perdew-Burke-Ernzerhof Functionals. *Phys. Rev. B* **1999**, *59*, 7413.
(57) Moellmann, J.; Grimme, S. DFT-D3 Study of Some Molecular Crystals. *J. Phys. Chem. C* **2014**, *118*, 7615−7621.
(58) Mahlberg, D.; Saking, S.; Forster-Tonigold, K.; Groß, A. Improved DFT adsorption energies with semiempirical dispersion corrections. *J. Chem. Theory Comput.* **2019**, *15*, 3250−3259.
(59) Wellendorff, J.; Lundgaard, K. T.; Møgelhøj, A.; Petzold, V.; Landis, D. D.; Nørskov, J. K.; et al. Density functionals for surface

https://dx.doi.org/10.1021/acs.chemmater.9b03686
Chem. Mater. XXXX, XXX, XXX−XXX

science: Exchange-correlation model development with Bayesian error estimation. *Phys. Rev. B* **2012**, *85*, No. 235149.
(60) Huang, M.; Fabris, S. CO adsorption and oxidation on ceria surfaces from DFT+*U* calculations. *J. Phys. Chem. C* **2008**, *112*, 8643−8648.
(61) Capdevila-Cortada, M.; Łodziana, Z.; Lo′pez, N. Performance of DFT+*U* approaches in the study of catalytic materials. *ACS Catal.* **2016**, *6*, 8370−8379.
(62) Ahmad, F.; Agusta, M. K.; Maezono, R.; Dipojono, H. K. DFT +*U* study of H_2O adsorption and dissociation on stoichiometric and nonstoichiometric CuO(111) surfaces. *J. Phys.: Condens. Matter* **2020**, *32*, No. 045001.
(63) Monkhorst, H. J.; Pack, J. D. Special Points for Brillonin-Zone Integrations. *Phys. Rev. B* **1976**, *13*, No. 5188.
(64) Clevert, D.; Unterthiner, T.; Hochreiter, S. Fast and Accurate Deep Network Learning by Exponential Linear Units (ELUs), 2015, arXiv:1511.07289. *arXiv preprint*. https://arxiv.org/abs/1511.07289 (accessed Dec 27, 2019).
(65) Kingma, D. P.; Ba, J. Adam: A method for stochastic optimization, 2014, arXiv:1412:6980. arXiv.org e-Print archive. https://arxiv.org/abs/1412.6980.
(66) Srivastava, N.; Hinton, G.; Krizhevsky, A.; Sutskever, I.; Salakhutdinov, R. Dropout: a simple way to prevent neural networks from overfitting. *J. Mach. Learn. Res.* **2014**, *15*, 1929−1958.

https://dx.doi.org/10.1021/acs.chemmater.9b03686
Chem. Mater. XXXX, XXX, XXX−XXX